Biogeochemical drivers of changing hypoxia in the California Current Ecosystem

R. Dussin[a,*], E.N. Curchitser[a], C.A. Stock[b], N. Van Oostende[c]

[a] *Department of Environmental Sciences, Rutgers University, New Jersey, USA*
[b] *NOAA Geophysical Fluid Dynamics Laboratory, New Jersey, USA*
[c] *Department of Geosciences, Princeton University, New Jersey, USA*

ABSTRACT

Recent observations have revealed significant fluctuations in near-shore hypoxia in the California Current Ecosystem (CCE). These fluctuations have been linked to changes in the biogeochemical properties (e.g. oxygen and nutrient contents) of the oceanic source waters of the California Current upwelling, and projections suggest the potential for decreased oxygen and increased nutrients in the source water under climate change. We examine both the separate and combined influences of these projected changes through a sequence of perturbation experiments using a regional coupled ocean dynamics/biogeochemistry (BGC) model of the CCE. The direct effect of a projected 5% decline in source water oxygen is to expand the hypoxic area by 12.5% in winter to 22.5% in summer. This exceeds the impact of a + 0.5% nitrate enrichment of source waters, which expands the hypoxic area by 6.5% to 12% via stimulation of nearshore Net Primary Productivity (NPP), increased organic matter export, and subsequent enhanced remineralization and dissolved oxygen (DO) consumption at depth. The combined effect of these perturbations consistently surpasses the sum of the individual impacts, leading to 20% to 32% more hypoxic area. The combined biogeochemical impact greatly exceeds the response resulting from a 10% strengthening in upwelling-favorable winds (+ 1% in hypoxic area) or the decreased oxygen solubility associated with a 2°C ocean warming (+ 3%). These results emphasize the importance of improved constraints on dynamic biogeochemical changes projected along the boundaries of shelf ecosystems. While such changes are often viewed as secondary impacts of climate change relative to local warming or stratification changes, they may prove dominant drivers of coastal ecosystem change.

1. Introduction

Due to decades of efforts monitoring dissolved oxygen (DO) concentration in the world's oceans, and building comprehensive observational databases, the scientific community has been able to observe a decline in DO over the past decades (Keeling et al., 2010; Helm et al., 2011; Schmidtko et al., 2017). Based on observations starting in the 1960s, Schmidtko et al. (2017) estimate the average decline to be of 2% over the past 50 years, corresponding to a total DO loss of 77 billion metric tons (Breitburg et al., 2018). Keeling and Garcia (2002) showed that the DO loss was the result of more complex processes than simply outgassing associated with decreased oxygen solubility of ocean waters as temperature increases, and must involve biological activity and water column stratification. Helm et al. (2011) estimate that only 15% of the DO decrease is the consequence of the reduced oxygen solubility of a warmer ocean mixed layer. The remaining 85% is then attributed to decreased ventilation of the ocean interior and the cumulative effects of respiration in less ventilated waters.

Decreased ventilation of ocean waters and the cumulative effects of respiration do not just reduce oxygen levels in interior waters. The remineralization of organic material associated with respiration releases nutrients that accumulate as oxygen declines. Upon eventual reintroduction to the euphotic zone, increased subsurface nutrients can enhance productivity (e.g. Rykaczewski and Dunne, 2010; John et al., 2015). Aerobic remineralization of the organic matter associated with this enhanced productivity after it sinks from the euphotic zone could exacerbate coastal eutrophication and hypoxia stress (Diaz and Rosenberg, 2008).

The California Current Ecosystem (CCE) is one of the major eastern boundary upwelling systems. Nutrient-rich subsurface waters brought up into the euphotic zone on the narrow CCE shelf create one of the most productive ecosystems in the world. However, the combined effect

---

of remineralization and low DO source waters leads to moderate to severe hypoxia on the shelf, particularly during the upwelling season. Emergence of previously unobserved hypoxic areas (Chan et al., 2008) and long-term declines in DO (Bograd et al., 2008) are raising concerns for CCE marine resources and the coastal economies they support.

Climate projections, based on Earth System Models (hereafter, ESMs), suggest the observed large-scale decline in DO over the last half century could continue into the 21st century (Bopp et al., 2013; Frölicher et al., 2009; Cocco et al., 2013). They project an additional 3 to 4% average loss in DO in the Representative Concentration Pathway (RCP) 8.5 (business as usual) climate change scenario. The DO decline as computed in ESMs over the past 50 years is about 4 times lower than the observational estimate (see Fig. 3 in Bopp et al., 2013). This suggests that there are still large uncertainties on the future rate of change of DO, with possible underestimation in ESMs. The North Pacific Ocean has been identified as one area where a large decline is expected (Bopp et al., 2013) due to a combination of warming, decreased ventilation, changing productivity and remineralization patterns (Cocco et al., 2013). Furthermore, Rykaczewski and Dunne (2010) predict, based on the GFDL ESM 2.1 climate model, that the nitrate enrichment of the upwelling source waters associated with decreased ventilation of North Pacific interior waters may increase the CCE productivity.

Assessing the consequences of the changes in ocean oxygen and nutrients described above on coastal hypoxia is hampered by the lack of horizontal resolution in current day ESMs. The typical 1° longitude/latitude horizontal resolution used in most global ESMs does not resolve the narrow shelf of the California Current and limits the ability of the model to adequately represent the coastal dynamics, such as upwelling, that are crucial for representing biological processes on the shelf (Stock et al., 2011). In order to overcome this problem, we use a high-resolution coupled ocean circulation and biogeochemical model of the CCE to investigate the relative magnitudes of the effects of potential oceanic oxygen and nitrogen changes on CCE coastal hypoxia. We further compare the imprint of dynamical ocean biogeochemical changes against impacts expected from 1) a warming induced change in oxygen solubility and 2) a hypothetical increase in upwelling favorable winds, which could also enhance hypoxia through enhanced supply of DO-depleted waters from the Oxygen Minimum Zone (Chan et al., 2008) and enhanced coastal production (Bakun et al., 2015).

2. Methods

2.1. The coupled biophysical model

We use the Regional Ocean Modeling System (ROMS, see Haidvogel et al. (2008) and Shchepetkin and McWilliams (2005) for details), coupled with the Carbon, Ocean Biogeochemistry and Lower Trophics (COBALT) model described in Stock et al. (2014). COBALT is a comprehensive BGC model resolving nitrate, phosphorus, iron, oxygen and carbon cycles. The lower trophic levels consist of 3 size classes for both phytoplankton and zooplankton. The addition of the third size class of phytoplankton, representing the chain-forming diatoms, to the original formulation of Stock et al. (2014) is described in Van Oostende et al. (2018). The ROMS implementation uses the Colella and Woodward (1984) algorithm for sinking organic matter, and air-sea gas exchange uses the piston velocity from Wanninkhof (1992) and neutral wind at 10 m height. Light penetration depends on the chlorophyll concentration, using the 2-band formulation from Manizza (2005) for the visible fraction of shortwave radiation, and partition between visible and near-infrared depends on the model prescribed Jerlov water type.

The California Current System model domain has a 7 km horizontal resolution and extends from the southern extent of the Baja California peninsula to Vancouver Island in the north; the cross-shore extent is approximately 1200 km (see Fig. 3). The model uses a third order upstream scheme for advection of momentum and a 4th-order centered horizontal advection scheme for all tracers. Mixing of momentum and

tracers is performed, respectively, along terrain-following surfaces and geopotentials. Dissipation and diffusion of momentum and tracers is achieved using a Laplacian operator with viscosity coefficient of $25 \, m^2. \, s^{-1}$ and diffusivity of $5 \, m^2. \, s^{-1}$. Bottom friction uses a quadratic formulation with a drag coefficient of $3e^{-3}$. Air-sea fluxes are computed using bulk formulae (Large and Yeager, 2004); the daily solar radiation is applied with an analytical diurnal cycle and there is a 90-day time-scale for the sea surface salinity restoring to the observed climatology.

2.2. Numerical experiments

To examine contributions of physical (ocean temperature, wind) and biogeochemical (oceanic DO and nutrient concentrations) changes on coastal hypoxia, we use a climate projection to create perturbations that will be added to a realistic present day baseline experiment. The reference numerical experiment (hereafter REF, Dussin et al., 2019a) is a 11-year long integration, starting from January 1996 (after a one year spin-up) and ending in December 2006. The atmospheric forcing is derived from the MERRA reanalysis (Rienecker et al., 2011). Boundary and initial conditions for the ocean dynamics are extracted from SODA 2.1.6 (Carton and Giese, 2008). Initial and boundary conditions for nitrate, phosphate, silica and oxygen concentrations are based on the 2013 World Ocean Atlas (hereafter WOA13) described in Garcia et al. (2014a) and Garcia et al. (2014b). Alkalinity and dissolved inorganic carbon are based on the Global Ocean Data Analysis Project (GLODAP, Key et al., 2004). Boundary and initial conditions for other plankton groups and nutrients are drawn from the global retrospective ocean-ecosystem simulation of Stock et al. (2014). River and coastal runoff are provided by the Dai and Trenberth (2002) dataset and remapped conservatively onto the regional domain and added as a freshwater source to the surface layer. The river input for nitrogen and phosphorus is obtained by multiplying the concentration of the various nutrients, taken from the global NEWS climatology (Seitzinger et al., 2005), by the total runoff and adding it to the surface layer.

Iron is not generally considered to be the primary limiting nutrient in the CCE and, in accordance with Rykaczewski and Dunne (2010), we thus focus on better characterized macronutrient perturbations in this work. Iron limitation can occur in the CCE, however, particularly on narrow to moderate width shelves, away from rivers, and/or where nitrogen is in excess (Hutchins et al., 1998; Till et al., 2018). Soluble iron dust inputs for all simulations herein are based on Moxim et al. (2011) and Fan et al. (2006). Sediment iron fluxes are based on Elrod et al. (2004), and scales in proportion to the flux of organic matter to the benthos. We include additional coastal iron source of similar magnitude, and specify a freshwater concentration of $15 \, \mu mol. \, m^{-3}$ (i.e. 15 nmol. L^{-1}). While dissolved iron concentrations within the Columbia River can be much greater than this (Fuhrer et al., 1996), much of this is lost to sedimentation. $15 \, \mu mol. \, m^{-3}$ was thus chosen to be consistent with the magnitude of peak river plume values within the coastal ocean (Chase, 2002, 2005; Lohan and Bruland, 2006).

To quantify the impact of the different contributors to coastal hypoxia under a climate change scenario, we carry out eight sensitivity experiments (see Table 1). Each sensitivity experiment explores the

Table 1
Description of the sensitivity experiments.

| Run	DO	Nutrients	Ocean temperature	Wind
O–N +	perturbed	perturbed	reference	reference
O-	perturbed	reference	reference	reference
N +	reference	perturbed	reference	reference
SOL-	reference	reference	perturbed	reference
W +	reference	reference	reference	perturbed
W + O–N +	perturbed	perturbed	reference	perturbed
W + O-	perturbed	reference	reference	perturbed
HD	half perturbed	half perturbed	reference	reference
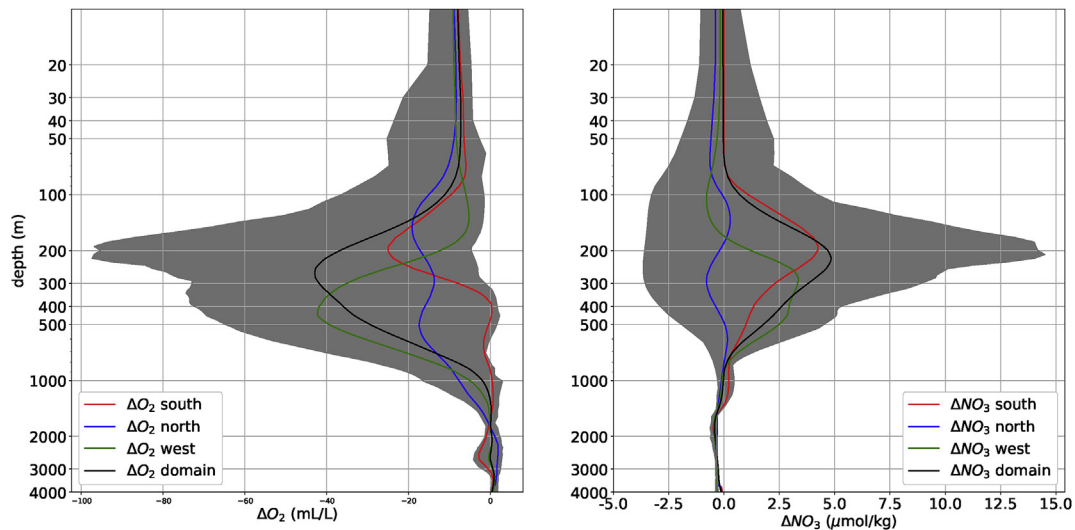
Fig. 1. Average profiles for DO *(left)* and nitrate *(right)* perturbations from ESM2M under the RCP 8.5 scenario. Red, blue and green shows the average profile at the southern, northern and western boundaries, respectively. Solid black is the domain average profile, with grey shading representing the range of values. (For interpretation of the references to color in this figure legend, the reader is referred to the Web version of this article.)

response of the system to one perturbation or to a combination. We examine the impact of perturbations coming from the biogeochemical properties of the off-shore source waters upwelled in the CCE in three experiments: one with a perturbation on DO only (hereafter O-, Dussin et al., 2019d), a second with perturbations on nutrients only (hereafter N+, Dussin et al., 2019c), and a third one combining both (O–N+, Dussin et al., 2019e). The perturbations are derived from a GFDL ESM2M climate projection under the RCP 8.5 scenario (Dunne et al., 2013), for which we compute the difference in nutrients (NO_3, PO_4 and SiO_4) and DO content between the last 30 years of the 21th and 20th centuries and apply them on both initial and boundary conditions individually or in a combination of perturbations in the various sensitivity experiments.

The perturbations provide an enhanced supply of nutrients and an oxygen depletion that extends roughly from 100 m down to 1000 m as shown by Fig. 1. The domain-averaged perturbations are maximum in the 200 to 300 m range, with values of -1 mL. L^{-1} and $+5\,\mu$mol. kg^{-1} for the DO and nitrate perturbations, respectively. Overall, the average (area weighted) nitrate in between 100 and 1000 m increases by 7% (1.68 μmol. kg^{-1}) while the average oxygen decreases by 19%. Perturbations are somewhat higher in the 100–500 m range, respectively $+20\%$ in nitrate and -21% in DO. The perturbation profiles at the southern boundary peak slightly higher in the water column than the domain average, while the western boundary profiles have a deeper maximum around 400 m. The northern boundary profiles are less pronounced, consistent with the subtropical origin of the perturbed water masses (see Fig. 2 in Rykaczewski and Dunne, 2010).

Fig. 2 shows the spatial structures of the DO and nitrate perturbations at 200 m, where the domain-averaged perturbation profiles are close to their maxima. The spatial structures of the perturbations show the expected anti-correlation between nitrate and DO (remineralization produces nitrate while consuming DO). The magnitude of the nitrate perturbation is maximum off the coast of southern California, reaching 15 μmol. kg^{-1}, then decreases sharply to half of its value by 35°N before stabilizing around 5 μmol. kg^{-1} farther north. The perturbation remains relatively homogeneous in the cross-shore direction in the first 500 km from the coast before decreasing farther away. The DO perturbation shows similar patterns of variation. At 100 m (black lines) and above, an upper ocean nitrate perturbation of lesser magnitude (2 to 3 μmol. kg^{-1}), originating from the North Pacific, enters the domain from the northern boundary. It is associated with a depletion of DO that extends down to the coast of northern California.

We compare the response driven by the DO and nutrient perturbations described above to several idealized perturbations. To compare against the direct effect of ocean temperature on oxygen solubility, we consider a case where the overall oxygen draw-down from saturation (i.e. the Apparent Oxygen Utilization, hereafter AOU) remains constant, but oxygen saturation is adjusted downward in a manner consistent with projected ESM2M warming. ESM2M projects a temperature increase of 2°C on average at the surface, then a sharp decrease with depth to 0. 5°C at 200 m before a secondary maximum of 1°C at 400 m and finally a decay to zero in the deep ocean. In the pseudo-experiment SOL-, we add this perturbation to the temperature of the REF experiment and recompute the solubility. By keeping the AOU constant, we obtain the updated DO from the direct ocean temperature change effect on ocean solubility.

Finally, we examine the response of an increase in upwelling-favorable wind in experiments W+ (Dussin et al., 2019f), W+O- (Dussin et al., 2019g) and W+O–N+ (Dussin et al., 2019h). In W+, we do not apply any changes to the source waters but add 10% to the meridional wind, over the whole domain, only when blowing southward from early June to late September. The timing of the perturbation follows results obtained by Snyder et al. (2003). The magnitude of the perturbation is chosen to be consistent with models projecting increases in upwelling strength under climate change. We note that the likelihood and mechanisms underlying such a potential increase are still subject to debate (Bakun, 1990; Sydeman et al., 2014; Rykaczewski et al., 2015). Our intent here is to solely test the implications of a hypothetical increase relative to the biogeochemical perturbations discussed above. Experiments W+O–N+ and W+O- are additional experiments assessing the impact of wind increase in combination with biogeochemical perturbations.

3. Results

3.1. Validation

Our regional high resolution physical-biological model is able to resolve many aspects of the CCE narrow coastal shelf dynamics, contrary to coarse resolution ESMs which lack horizontal resolution to accurately represent them. Fig. 3 illustrates the modeled spatial structures for SST and chlorophyll concentration ([Chl]) during the summer months, when the upwelling is well established. In the left panel of Fig. 3, we compare our high resolution REF experiment with ESM2M
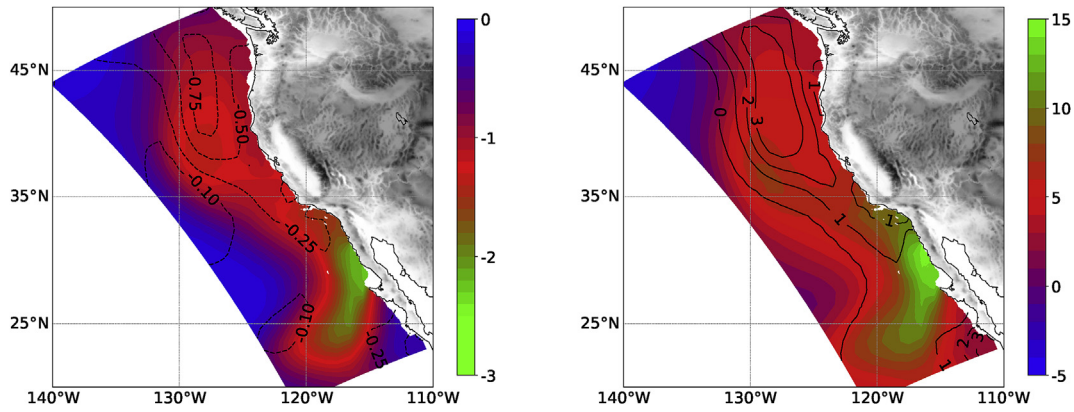
Fig. 2. Colored contours show the spatial distribution of DO (mL.L^{-1}, *left panel*) and nitrate (μmol. kg^{-1}, *right panel*) perturbations at 200 m from ESM2M under the RCP 8.5 scenario. Colormaps are reversed in sign to better demonstrate the anti-correlation. Superimposed black contours show the DO and nitrate values at 100 m.

and observations: NOAA OISST (Reynolds et al., 2002) for SST and SeaWIFS (NASA Ocean Biology Processing Group, 2015) for [Chl] in the core of the upwelling, between 34. 5°N and 44°N at the coast. While SST in ESM2M remains within a 1°C range in the first 500 km to the coast, the REF experiment shows a 6°C decrease towards the coast. Although the model SST is biased warm by 1 to 2°C, the temperature of the up-welled waters is in agreement with observed values. Consequently, the vertical supply of nutrients in ROMS is greatly improved and the [Chl] solution is more realistic than ESM2M, reproducing the elevated [Chl] at the coast, as given by the SeaWIFS estimates. Although the [Chl] transition from the highly productive shelf to the oligotrophic gyre is too sharp, the primary area of interest for hypoxia lies before this transition, at depths < 500 m within 25 km of the coast.

We assess the DO fidelity with two metrics central to our perturbation study: 1) the depth of the hypoxic boundary; and 2) the near-bottom DO on the shelf. We define hypoxia using a threshold of 1.43 mL/L (i.e. 61.7 μmol/kg), similar to Van Oostende et al. (2018). The hypoxic boundary is the surface separating the hypoxic waters from well-oxygenated waters on top of them. It is a convenient measure for available habitat for pelagic fish species along the water column (Bograd et al., 2008). Fig. 4 shows the modeled hypoxic boundary depth in the REF experiment compared to the one derived from the WOA13 climatology. This boundary is shallower than 100 m in the southernmost part of the domain and deepens towards the northwest

and can reach up to 600 m. The hypoxic boundary remains stable throughout the seasonal cycle (standard deviation between 5 and 15 m offshore and can reach 20 to 25 m at the coast where the upwelling is strong). In our region of primary interest (the CCE upwelling region between the black dashed lines), the model is able to reproduce the large-scale structure of the hypoxic boundary and has an area-weighted average bias of 20 m shallower with local differences ranging from 70 m shallower to 30 m deeper. Major differences are located in the narrow band of intense coastal upwelling, where WOA13 1° horizontal resolution cannot represent this level of detail.

To evaluate the quality of the model's bottom DO solution, we compare the REF experiment with the field observations of near-bottom DO provided by NOAA's Northwest Fisheries Center, collected between 2009 and 2015 and described in Keller et al. (2015). Fig. 5 shows the near-bottom DO as a function of depth on the shelf and continental slope for the months of June, July and August. Observations (red dots) show the rapid decline of near-bottom DO content with bottom depth and the presence of shallow hypoxic zones. These shallow hypoxic zones are of great importance because variation in the area they occupy is going to greatly influence which fraction of the shelf becomes un-available as a habitat for macrofauna (e.g. bottom dwelling fish, crabs, etc.). Near-bottom DO measurements deeper than 500 m are consistently far below the hypoxic threshold, which stresses the importance of the upper 500 m to support benthic fisheries reliant on aerobic
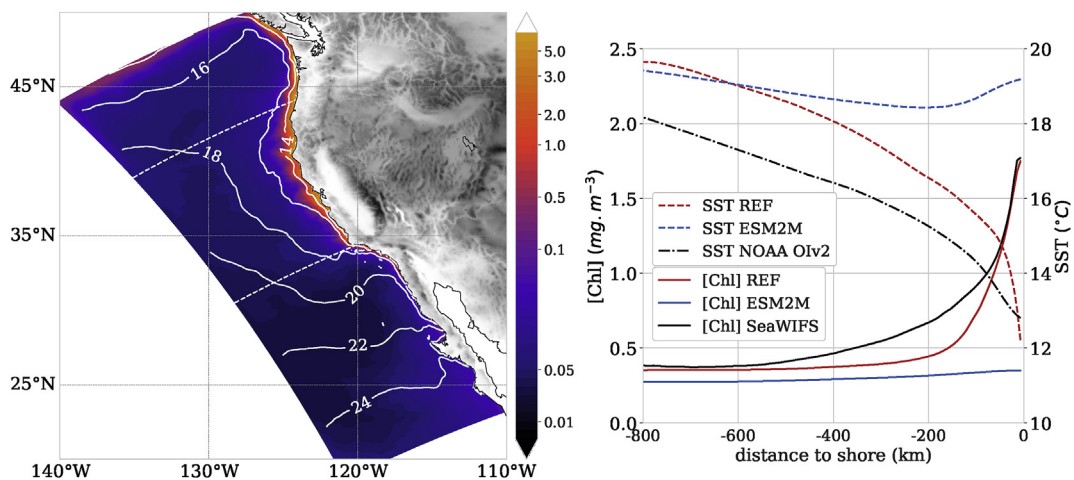

Fig. 3. *left:* Summer (JJA) surface [Chl] (mg/m³) averaged over the 1996–2006 period in the REF experiment. White solid contours are showing SST for the same period. White dashed lines, originating from the coast at 34. 5°N and 44°N, are the spatial bounds of integration used in the right panel. *right:* Cross-shore summer surface [Chl] and SST in REF experiment for 1996–2006, ESM2M climate model and Observations (SeaWIFS and NOAA OISST respectively). Due to the varying depth of the terrain-following coordinate, SST and [Chl] in ROMS are integrated over the first 10 m, which corresponds to the first layer of ESM2M. Data are then averaged alongshore between the bounds shown on the left panel.
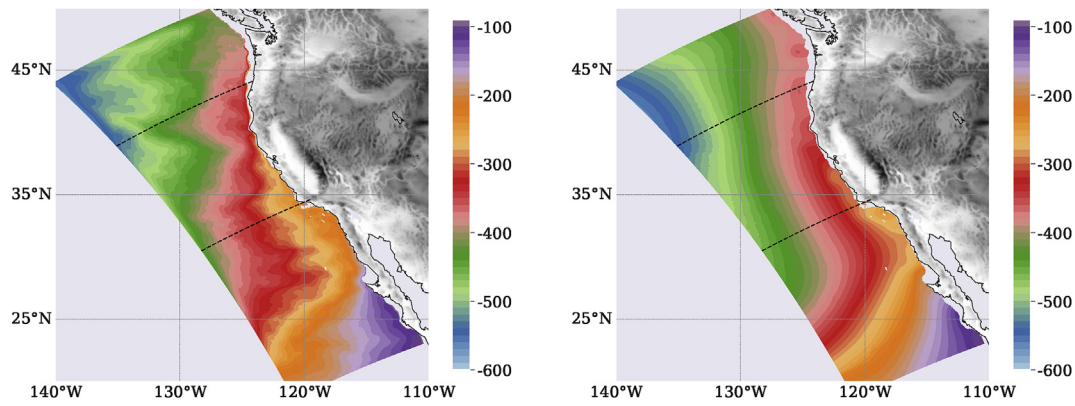
Fig. 4. Depth (m) of the hypoxic boundary, averaged over 1996–2006, in REF experiment *(left)* compared to the annual climatology of World Ocean Atlas (2013) *(right)*. Waters deeper than the hypoxic boundary have DO<1.43 mL. L^{-1}.
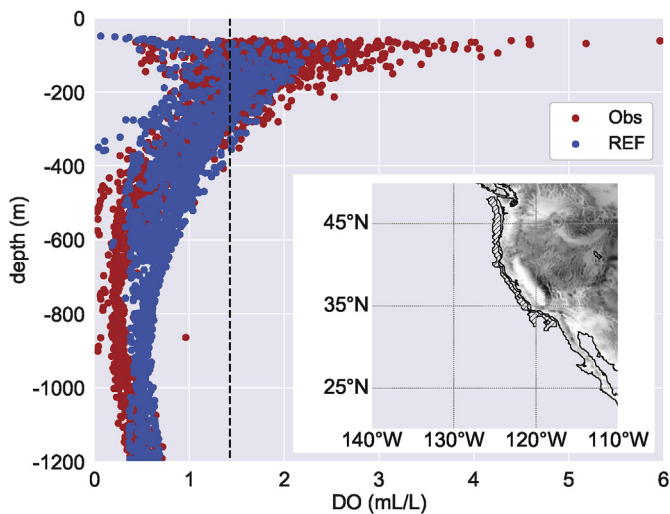

Fig. 5. Near-bottom dissolved oxygen (DO) in REF experiment compared to observations from NOAA Northwest Fisheries Center collected between 2009 and 2015. Model monthly averages for 1996–2006 are projected onto the observation locations of the corresponding month, from June to August. Shaded black contour in the inserted map shows the area where the near-bottom dissolved oxygen (DO) observations were collected.

conditions. The time-averaged solution from the REF experiment is projected onto the observations points for each month (blue dots in Fig. 5). The obtained profile is in good agreement with the observations: the model is able to reproduce the near-bottom DO decline with depth and its feature of shallow hypoxic zones. The near-bottom DO content between 700 m and 1000 m is slightly over-estimated, but all values in this depth range for both the model and the observations fall below the hypoxic threshold. This bias will thus not effect the hypoxic metrics in the analysis.

3.2. Hypoxia response to physical and biogeochemical perturbations

We begin our hypoxia sensitivity analysis with the perturbation of primary production (Fig. 6), which determines the potential supply of organic matter to the benthos. Net primary production during the summer upwelling period peaks at 2500 mgC. m^{-2}. day^{-1} in REF, consistent with peak observed and satellite-based NPP estimates (Kahru et al., 2009). The various sensitivity experiments show that an increase in nutrient supply, either through the biogeochemical perturbation or increased winds, produces an increase of up to 500 mgC. m^{-2}. day^{-1}. This represents between 10 and 20% of the coastal NPP in the REF simulation. Reduced oxygen alone (O-) has the least effect on NPP among

the experiments.

Further inspection of the wind and nutrient perturbations reveals latitudinal contrasts in the O–N+, N+ and W+ NPP responses. While these are secondary to the differences between these three cases and O-, they are nonetheless notable. The W+ experiment leads to a greater increase in the NPP along northern California and Oregon, where the coastline is almost parallel to the meridian. The N+ perturbation has a greater effect south of 38°N. This reflects a moderating effect of mild iron limitation off Oregon in the model (in a manner consistent with Till et al., 2018). The O–N+ perturbation has a somewhat stronger NPP response, with values greater than 250 mgC. m^{-2}. day^{-1} extending farther north along the coast to 41. 5°N. As we will discuss in Section 4, this is due to a weak feedback between increasing hypoxia in this run, increased detrital flux to the benthos, and increased iron flux from the benthos.

The changes in NPP in Fig. 6 are reflected in enhanced export at 100 m. Fig. 7 shows the cross-shore structure of the anomalies between the sensitivity experiments and the baseline for NPP and export flux at 100 m. Once again, the primary contrast is between O-, which produces little change in export, and the other perturbations. The W+ experiment, however, also shows an interesting contrast with the N+ and O–N+ experiments in that export is actually reduced at the coast before being enhanced in a wide off-shore band. This reflects increased offshore Ekman transport. The wind perturbation creates a deficit of export flux at 100 m in June (not shown) between − 40 mgC. m^{-2}. day^{-1} at the coast and − 10 mgC. m^2. day^{-1} 25 km from shore. Between 50 and 150 km the export flux is increased by 35 to 39 mgC. m^2. day^{-1}, which could have contributed to bottom hypoxia had the central CCE shelf been broader. This effect is partially revealed by the W+ export flux summer anomaly, in which the coastal value of the export flux anomaly is negative. The N+ and O–N+ perturbations, which are not subject to the enhanced off-shore Ekman transport of W+, feature narrower but more intense bands of enhanced export with increases even in the immediate vicinity of the coast.

To quantify the projected effects of hypoxia drivers on habitat availability, we compute the change in depth of the hypoxic boundary (isosurface of DO = 1.43mL. L^{-1}) and the change in the fraction of hypoxic area on the shelf, derived from the modeled near-bottom DO. Fig. 8 shows the difference in depth of the hypoxic boundary between experiments O–N+ and REF (shown in Fig. 4), computed over the 1996–2006 interannual average. Under this scenario, the hypoxic boundary would shoal significantly off the coast of northern California, Oregon and Washington. Except for the northernmost and southernmost fractions of the domain, the coastal waters, within the first 500 km, are experiencing a shoaling greater than 50 m and up to 140 m. Averaged over the first 500 km from the coast, the mean value of the shoaling for perturbation O–N+ is of 53 m. This represents a loss of 18% of water volume above the hypoxic threshold. This loss can be greater
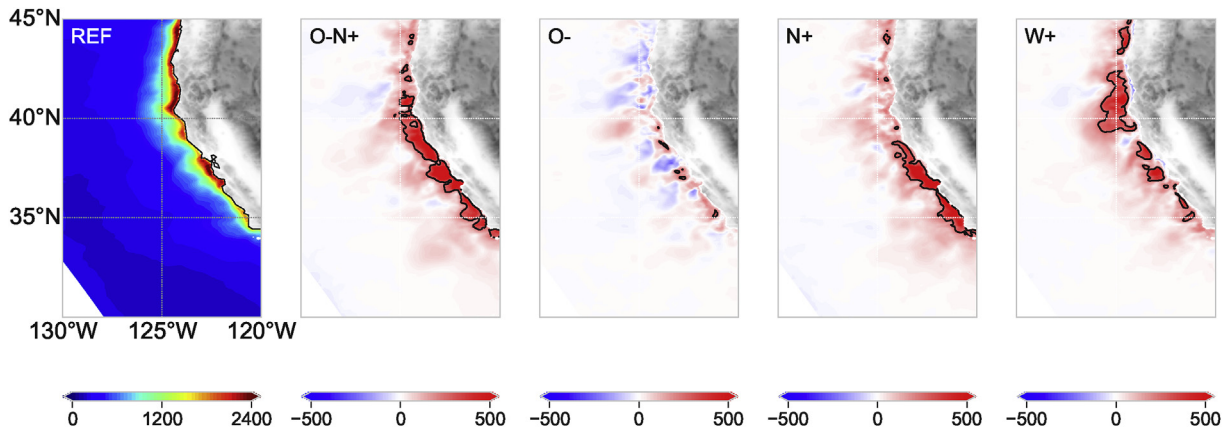
R. Dussin, et al.

Fig. 6. *REF:* average summer NPP (mgC.m⁻². day⁻¹) in REF experiment *O–N+, O-, N+, W+ :* difference to REF in all four sensitivity experiments. Contoured value is 250 mgC. m⁻². day⁻¹.
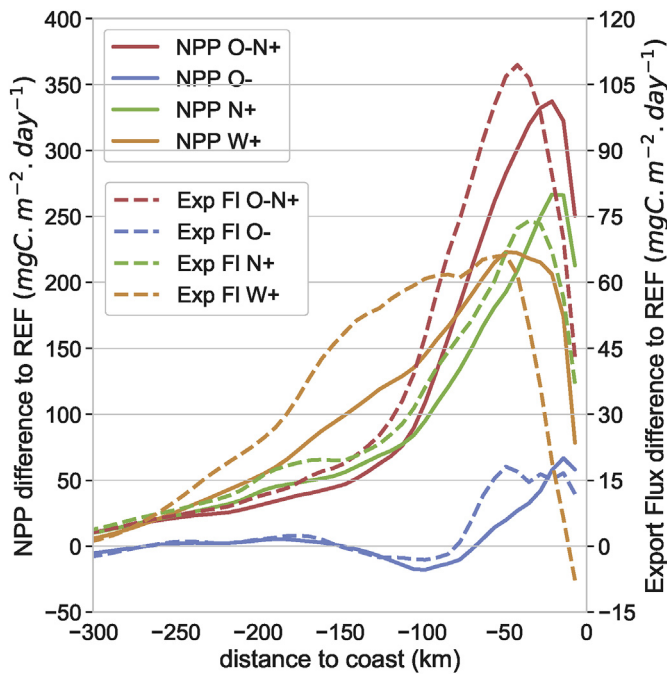
Fig. 7. NPP and Export flux at 100 m difference to REF summer average (mgC.m⁻². day⁻¹). Cross sections are computed between the bounds defined in Fig. 3.

locally and ranges between 20% and 25% in the area comprised between 33°N and 45°N. This change remains consistent throughout the seasonal cycle.

To compare shoaling in the different perturbations, we averaged the depth of the hypoxic boundary in the first 500 km from the coast in one degree latitude bins. This is shown on the right panel of Fig. 8. The projected shoaling in the O- experiment share the same spatial structure as O–N+ and reaches 80% of the magnitude of the O–N+ experiment. The O- perturbation is thus the major contributor to the shoaling of the hypoxic boundary. Perturbations that do not include O- have a much weaker impact on the depth of the hypoxic boundary (Fig. 8, right panel). In particular, the wind perturbation added to both the reference (W+) and biogeochemically perturbed states (W+O–N+ and W+O-) is of secondary importance compared to biogeochemical perturbations. We will discuss this point in Section 4.

We assess the effect of perturbations on the available aerobic habitat for benthic communities on the shelf by computing how much the hypoxic area is projected to spread. Fig. 5 shows that, based on the bottom DO observations, areas deeper than 500 m are hypoxic. We thus focus the analysis on the section of the shelf between the coast and the 500 m isobath. Fig. 9 shows the percentage of the shelf that is hypoxic in the REF experiment with bars showing by how much this would increase under the perturbations scenarios. The fraction of hypoxic area in the REF experiment seasonally varies between 45 and 70%, with a maximum in late spring/early summer, that corresponds to the core of the upwelling season. Under the combined O–N+ perturbation, the hypoxic area increases by 20 to 32% and reaches 97% in May/June. Broken
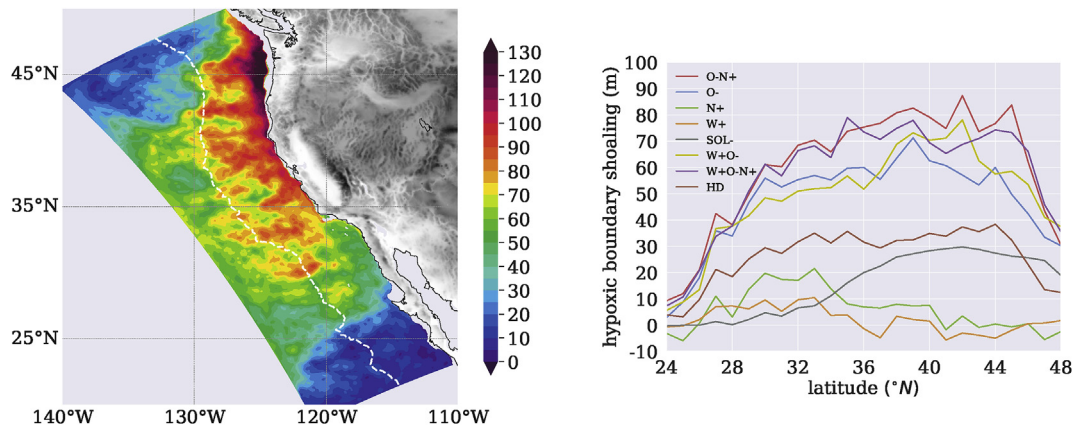

Fig. 8. *left:* Change in the depth (m) of the hypoxic boundary between experiment O–N+ and REF. Positive values represent an increase of hypoxic water volume as the depth of the hypoxic boundary shoals. Non-colored areas near the shore are above hypoxic threshold at all depth. Dashed white line represents the 500 km distance to the coast. *right:* Corresponding zonal average in one degree of latitude bins, from coastline to 500 km offshore in all sensitivity experiments.
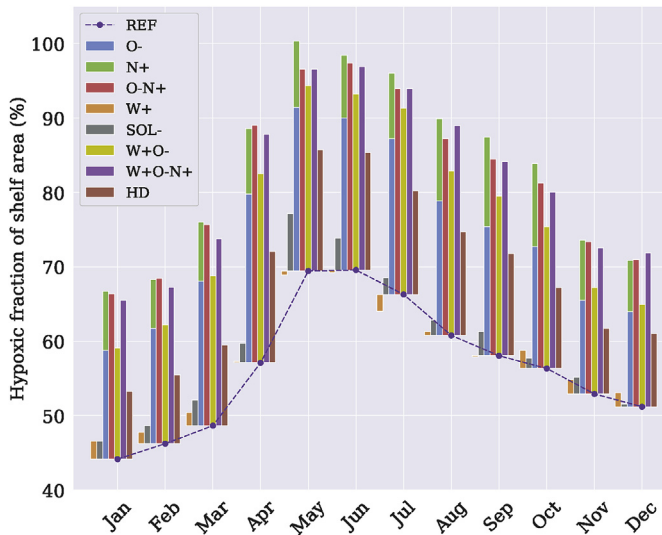
Fig. 9. Mean hypoxic area on the shelf (defined from the coast to the 500 m isobath, between 34. 5°N and 44°N) in reference and sensitivity experiments. Data are averaged monthly for 1996–2006.

down by individual perturbations, O- perturbation adds 12.5 to 22.5% hypoxia to the system, while N + perturbation only adds 6.5 to 12%. It is worth noting that the response to the combined perturbation does not equal the sum of responses to individual perturbation, due to non-linear interactions with the iron limitation (see discussion of the NPP response, Section 4). Our results suggest that, in the considered future projection, changes in hypoxia on the shelf result mainly from deoxygenation of source waters. The nutrient enrichment and subsequently enhanced organic matter remineralization from these waters are secondary, but yet still significant, contributors.

The physical processes considered (the direct effect of temperature on oxygen solubility, stronger upwelling winds) have lower impacts than deoxygenation on the spread of coastal hypoxia. Experiment SOL- yields an average increase in hypoxic area of 3%, peaking during the upwelling season. The wind-driven perturbation produces an even lower increase in hypoxic area of 1%. Interestingly, this minor impact occurs despite increased upwelling winds enhancing nutrients delivered to the surface to a similar degree as the N + perturbation, which produce on average a 9% increase in hypoxic area. The contrast reflects differences in ocean circulation: in experiment W +, the particulate organic matter (POM) present on the shelf is flushed offshore by the onset of the stronger upwelling circulation starting in June. This leads to a reduction of the export flux on the shelf during the summer months (Fig. 7) and particularly in June, which in turn slightly reduces the coastal hypoxia in June and July (see Fig. 9). The additional export fluxes for the rest of the year only contribute weakly to hypoxia. The narrow topography of the CCE shelf plays an important role in this local phenomenon: because the average distance to the coast of the 500 m isobath is only 25 km, even a slight displacement of the export flux offshore is enough to make the POM sink to bottom waters that are already hypoxic. The results obtained in experiments W + O–N + and W + O- are very similar to O–N + and O-, hinting again at a smaller impact of the wind perturbation, this will be discussed in Section 4.

4. Discussion

Using a 7 km horizontal resolution regional model of the CCE, we investigate the drivers of coastal hypoxia by perturbing key physical and biogeochemical variables which are expected to change in the near future. Rykaczewski and Dunne (2010) showed the implications of projected changes in the ocean water masses on the productivity in the CCE. However, their climate model's spatial resolution did not allow a

detailed look at the shelf properties. Using perturbations of nutrients and DO fields from an ESM in our regional model, we show that the projected deoxygenation and nutrient enrichment of source waters would result in a significant expansion of hypoxic areas on the CCE shelf. While both perturbations on nutrients and DO contributed to expanded hypoxia, the effect of decreased source water DO was 2 times larger than increased nutrients.

Nutrient supply plays a major role in the ecosystem dynamics, sustaining productivity but also increasing remineralization and consuming oxygen when nutrient supply is increased. Eutrophication associated with enhanced nutrient inputs from rivers and terrestrial sources has contributed to increased hypoxia in many coastal areas (Diaz and Rosenberg, 2008; Breitburg et al., 2018). Increased nutrient concentrations in offshore waters flowing into coastal areas could further exacerbate this issue.

We show here that global deoxygenation should not be overlooked as a driver of coastal hypoxia expansion. The subsurface DO content depends on the water mass history. Climate projections (Bopp et al., 2013; Cocco et al., 2013) suggests that the deoxygenation trend will continue over the 21st century as a result of reduced solubility due to increasing ocean temperature, reduced ventilation (Helm et al., 2011), enhanced DO utilization from increased biological rates (Breitburg et al., 2018) and changes in circulation that extend the age of the water masses (Rykaczewski and Dunne, 2010). We show that these remote processes controlling DO can potentially have a greater impact on coastal hypoxia than the local solubility loss due to increasing water temperature. Unfortunately, global deoxygenation of the ocean poses a great challenge to stop or reverse it. However, reducing the nutrient input into the coastal waters, resulting from human activities, can be addressed on a more local scale and can have a significant impact on the occurrence of coastal hypoxia.

It is notable that the nutrient perturbations herein focused on macronutrient perturbation, in accordance with the results of Rykaczewski and Dunne (2010) and the assumption that nitrogen is the primary limiting nutrient in the CCE. Growing evidence, however, suggests a "mosaic" of iron and nitrogen limitations (Hutchins et al., 1998; Till et al., 2018), with iron limitation most likely on narrow shelves, away from river inputs, and/or in areas where other nutrients are replete. The REF simulation herein exhibited mild iron limitation in nitrogen rich waters adjacent to the Oregon and northern California coast during the summer upwelling/low rainfall period, consistent with these expectations. In the N + experiment, this iron limitation muted the near-shore NPP response in the northern part of the central CCE. In the O–N + case, reduced remineralization rates in increasingly hypoxic waters increased the detrital flux reaching the benthos. In accordance with Elrod et al. (2004), this enhanced the iron supply from the sediment. The uncertainty surrounding such feedbacks, however, remains high (Dale et al., 2015), as does the uncertainty in many aspects of the iron cycle and models of it (Tagliabue et al., 2016, 2017). The effect of iron in our simulation was secondary to the overall contrasts between the N +, O-, W + and SOL-responses, but the significance of the response underlines the importance of more complete understanding of the iron cycle and its sensitivity to climate change in order to form a complete picture of the response of the CCE to climate drivers.

An increase in upwelling-favorable winds is cited as a potential factor in increasing NPP and coastal hypoxia (Bakun et al., 2015). With a simple, magnitude based approach for our upwelling-favorable wind perturbation, we obtain a significant increase in NPP that is the same order of magnitude as the nutrient enrichment experiment. However, we do not detect an impact on coastal hypoxia because of the timing and topography of the coastal upwelling system. The increased winds during the upwelling season results in a temporary displacement of the export flux offshore from the narrow shelf of the CCE. It is notable that the horizontal resolution of the MERRA wind forcing (0.5 × 0.66°) does not capture the details of coastal dynamics, especially wind stress drop-off at the coast. The underestimation of the wind stress curl leads to a

weaker Ekman pumping, and hence favors a more intense and localized coastal upwelling (Capet et al., 2004; Jacox and Edwards, 2012). This also has repercussions on the depth of the upwelling cell as well as changes in the structure of the poleward/equatorward coastal current system (Song et al., 2011). These complex dynamics can influence the depth of origin of the source waters and consequently the nutrient content.

Renault et al. (2016) have demonstrated the decoupling of the NPP to the cross-shore structure of the wind stress curl. In their study, the wider wind coastal drop-off (100 km) leads to an increased NPP compared to the linear and sharp drop-off cases. Different choices regarding the wind perturbation could lead to different magnitudes and/or spatial structures of the enhanced NPP. However, the associated strengthening of the Ekman transport would also shift nutrients, production and export offshore and may result in a similar effect on coastal hypoxia than our simple perturbation. It is worth noting that the intensification of upwelling favorable winds is still subject to discussion (Rykaczewski et al., 2015; Bakun et al., 2015).

To confirm the relative importance of wind and biogeochemical perturbations, we discuss the results of two more experiments (W+O- and W+O–N+) in which the wind perturbation is added to experiments O- and O–N+. These experiments confirm the first order role of the biogeochemical pertubations. Shoaling of the hypoxic boundary tracks closely with their non wind-perturbed counterparts, especially south of 36°N. North of this latitude, the W+O- experiment exhibits slightly shallower hypoxic boundary (up to 20 m locally but on average close to 10 m), which is consistent with enhanced supply of nutrients brought into the euphotic zone by increased upwelling. However, in the W+O–N+ experiment, the effect of the wind is to decrease by 1.4% (i.e. 4 m) the shoaling north of 36°N. This could be due to increased Ekman transport flushing the nutrients off the shelf, as described in experiment W+. On the shelf, the addition of the wind perturbation in W+O- produces an additional 2% hypoxic area on average compared to O-, with monthly values ranging between 0 and 4%. In the W+O–N+ case, this change is reduced to − 0.45% with monthly values between − 2 and 2%.

To assess the sensitivity of these hypoxia metrics to the magnitude of the perturbations, we add a final experiment in which only half of the magnitude of the perturbations on DO and nutrients is applied (HD, Dussin et al., 2019b). The obtained amplitude changes in both shoaling of the hypoxic boundary and hypoxic area on the shelf were close to half of what we obtain with the full perturbation O–N+. This behavior is unexpected given that the metrics used are based on a threshold response and hence highly nonlinear. For example, doubling the perturbation could not lead to twice the results obtained in O–N+ since the metrics would reach their saturation value. In order to determine clearly the linearity or not of the system, more than two experiments would be necessary to properly compute the rate of change of our metrics to the change in perturbations. However, this comparison can provide a scaling of the expected magnitude of our hypoxic metrics given a range of perturbations between the half and full perturbation.

There are still large discrepancies between ESM projections leading to uncertainties on the fate of nutrients, DO, and subsequent ecosystem responses (Frölicher et al., 2016). Hence this perturbation study, examining the relative contributions of BGC and physical stressors in one possible scenario, suggests that biogeochemical perturbations could be first order effects. The assumption made here, that the atmospheric and oceanic circulation and water masses properties will remain similar to those of the 20th century, could influence the magnitude of our estimates of hypoxic boundary displacement. Here we did not consider future changes to ocean stratification, which are known to impact the depth of upwelling source waters (Jacox and Edwards, 2011). Projected changes in atmospheric and oceanic circulation can also have an impact on the coastal ecosystem as it is sensitive to both mesoscale eddies (Xiu et al., 2018) and interannual variability such as the El Niño Southern Oscillation (Jacox et al., 2015; Turi et al., 2018) or North Pacific Gyre Oscillation (Chenillat et al., 2012).

The perturbed experiment O–N+ demonstrates consistent results with the NPP obtained from the fully coupled climate model projection of Rykaczewski and Dunne (2010). However the goal of this study is not to provide a comprehensive projection of the CCE ecosystem status at the end of the 21st century. Rather, our intent is to assess the potential importance and interactions through a series of idealized perturbations, similar to other recently published works (e.g. Irby, 2018). Our regional modeling approach has advanced our understanding of the relative importance of various physical and biogeochemical drivers on coastal hypoxia, despite the inherent complexity of the climate system and its interactions. To obtain a more realistic estimate of the coastal hypoxia, one would need to force the regional model with both atmospheric conditions, ocean physics and BGC obtained from an ESM. Such a downscaling could be of great use to predict future habitat changes and its economic impacts.

Appendix A. Supplementary data

Supplementary data to this article can be found online at https://doi.org/10.1016/j.dsr2.2019.05.013.

References

Bakun, A., 1990. Global climate change and intensification of coastal ocean upwelling. Science 247, 198–201. https://doi.org/10.1126/science.247.4939.198. URL. https://science.sciencemag.org/content/247/4939/198.

Bakun, A., Black, B.A., Bograd, S.J., García-Reyes, M., Miller, A.J., Rykaczewski, R.R., Sydeman, W.J., 2015. Anticipated effects of climate change on coastal upwelling ecosystems. Curr. Clim. Change Rep. 1, 85–93. https://doi.org/10.1007/s40641-015-0008-4. URL: http://link.springer.com/10.1007/s40641-015-0008-4.

Bograd, S.J., Castro, C.G., Di Lorenzo, E., Palacios, D.M., Bailey, H., Gilly, W., Chavez, F.P., 2008. Oxygen declines and the shoaling of the hypoxic boundary in the California current: hypoxia in the California current. Geophys. Res. Lett. 35, L12607. https://doi.org/10.1029/2008GL034185. URL: http://doi.wiley.com/10.1029/2008GL034185.

Bopp, L., Resplandy, L., Orr, J.C., Doney, S.C., Dunne, J.P., Gehlen, M., Halloran, P., Heinze, C., Ilyina, T., Séférian, R., Tjiputra, J., Vichi, M., 2013. Multiple stressors of ocean ecosystems in the 21st century: projections with CMIP5 models. Biogeosciences 10, 6225–6245. https://doi.org/10.5194/bg-10-6225-2013. URL: http://www.biogeosciences.net/10/6225/2013/.

Breitburg, D., Levin, L.A., Oschlies, A., Grégoire, M., Chavez, F.P., Conley, D.J., Garçon, V., Gilbert, D., Gutiérrez, D., Isensee, K., Jacinto, G.S., Limburg, K.E., Montes, I., Naqvi, S.W.A., Pitcher, G.C., Rabalais, N.N., Roman, M.R., Rose, K.A., Seibel, B.A., Telszewski, M., Yasuhara, M., Zhang, J., 2018. Declining oxygen in the global ocean and coastal waters. Science 359, eaam7240. https://doi.org/10.1126/science.aam7240. URL: http://www.sciencemag.org/lookup/doi/10.1126/science.aam7240.

Capet, X.J., Marchesiello, P., McWilliams, J.C., 2004. Upwelling response to coastal wind profiles. Geophys. Res. Lett. 31, L13311. https://doi.org/10.1029/2004GL020123. URL: http://doi.wiley.com/10.1029/2004GL020123.

Carton, J.A., Giese, B.S., 2008. A reanalysis of ocean climate using simple Ocean Data assimilation (SODA). Mon. Weather Rev. 136, 2999–3017. https://doi.org/10.1175/2007MWR1978.1. URL: http://journals.ametsoc.org/doi/abs/10.1175/2007MWR1978.1.

Chan, F., Barth, J.A., Lubchenco, J., Kirincich, A., Weeks, H., Peterson, W.T., Menge, B.A., 2008. Emergence of anoxia in the California current large marine ecosystem. Science 319https://doi.org/10.1126/science.1149016. 920–920. http://www.sciencemag.org/cgi/doi/10.1126/science.1149016 URL:.

Chase, Z., 2002. Iron, nutrient, and phytoplankton distributions in Oregon coastal waters.

J. Geophys. Res. 107, 3174. https://doi.org/10.1029/2001JC000987. URL: http://doi.wiley.com/10.1029/2001JC000987.

Chase, Z., 2005. Distribution and variability of iron input to Oregon coastal waters during the upwelling season. J. Geophys. Res. 110, C10S12. https://doi.org/10.1029/2004JC002590. URL: http://doi.wiley.com/10.1029/2004JC002590.

Chenillat, F., Rivière, P., Capet, X., Di Lorenzo, E., Blanke, B., 2012. North pacific gyre oscillation modulates seasonal timing and ecosystem functioning in the California current upwelling system: npgo and California upwelling onset. Geophys. Res. Lett. 39, L01606. https://doi.org/10.1029/2011GL049966. URL: http://doi.wiley.com/10.1029/2011GL049966.

Cocco, V., Joos, F., Steinacher, M., Frölicher, T.L., Bopp, L., Dunne, J., Gehlen, M., Heinze, C., Orr, J., Oschlies, A., Schneider, B., Segschneider, J., Tjiputra, J., 2013. Oxygen and indicators of stress for marine life in multi-model global warming projections. Biogeosciences 10, 1849–1868. https://doi.org/10.5194/bg-10-1849-2013. URL: http://www.biogeosciences.net/10/1849/2013/.

Colella, P., Woodward, P.R., 1984. The piecewise parabolic method (PPM) for gas-dynamical simulations. J. Comput. Phys. 54, 174–201. https://doi.org/10.1016/0021-9991(84)90143-8. URL: http://linkinghub.elsevier.com/retrieve/pii/0021999184901438.

Dai, A., Trenberth, K.E., 2002. Estimates of freshwater discharge from continents: latitudinal and seasonal variations. J. Hydrometeorol. 3, 660–687. https://doi.org/10.1175/1525-7541. URL: http://journals.ametsoc.org/doi/abs/10.1175/1525-7541%282002%29003%3C0660%3AEOFDFC%3E2.0.CO%3B2 (2002) 003 < 0660:EOFDFC > 2.0.CO;2.

Dale, A.W., Nickelsen, L., Scholz, F., Hensen, C., Oschlies, A., Wallmann, K., 2015. A revised global estimate of dissolved iron fluxes from marine sediments: global benthic iron fluxes. Glob. Biogeochem. Cycles 29, 691–707. https://doi.org/10.1002/2014GB005017. URL: http://doi.wiley.com/10.1002/2014GB005017.

Diaz, R.J., Rosenberg, R., 2008. Spreading dead zones and consequences for marine ecosystems. Science 321, 926–929. https://doi.org/10.1126/science.1156401. URL: http://www.sciencemag.org/cgi/doi/10.1126/science.1156401.

Dunne, J.P., John, J.G., Shevliakova, E., Stouffer, R.J., Krasting, J.P., Malyshev, S.L., Milly, P.C.D., Sentman, L.T., Adcroft, A.J., Cooke, W., Dunne, K.A., Griffies, S.M., Hallberg, R.W., Harrison, M.J., Levy, H., Wittenberg, A.T., Phillips, P.J., Zadeh, N., 2013. GFDL's ESM2 global coupled climate–carbon earth system models. Part II: carbon system formulation and baseline simulation characteristics*. J. Clim. 26, 2247–2267. https://doi.org/10.1175/JCLI-D-12-00150.1. URL: http://journals.ametsoc.org/doi/abs/10.1175/JCLI-D-12-00150.1.

Dussin, R., Curchitser, E., Stock, C.A., Van Oostende, N., 2019a. 10 years average run 3ps. https://doi.org/10.6084/m9.figshare.7914461.v2. URL: https://figshare.com/articles/10_years_average_run_3PS/7914461/2.

Dussin, R., Curchitser, E., Stock, C.A., Van Oostende, N., 2019b. 10 years average run hd. https://doi.org/10.6084/m9.figshare.7914413.v2. URL: https://figshare.com/articles/10_years_average_run_HD/7914413/2.

Dussin, R., Curchitser, E., Stock, C.A., Van Oostende, N., 2019c. 10 years average run n+. https://doi.org/10.6084/m9.figshare.7914323.v2. URL: https://figshare.com/articles/10_years_average_run_N/7914323/2.

Dussin, R., Curchitser, E., Stock, C.A., Van Oostende, N., 2019d. 10 years average run o-. https://doi.org/10.6084/m9.figshare.7914299.v2. URL: https://figshare.com/articles/10_years_average_run_O-/7914299/2.

Dussin, R., Curchitser, E., Stock, C.A., Van Oostende, N., 2019e. 10 years average run o-n+. https://doi.org/10.6084/m9.figshare.7897604.v2. URL: https://figshare.com/articles/10_years_average_run_O-N_/7897604/2.

Dussin, R., Curchitser, E., Stock, C.A., Van Oostende, N., 2019f. 10 years average run w+. https://doi.org/10.6084/m9.figshare.7914347.v2. URL: https://figshare.com/articles/10_years_average_run_W_/7914347/2.

Dussin, R., Curchitser, E., Stock, C.A., Van Oostende, N., 2019g. 10 years average run w+o-. https://doi.org/10.6084/m9.figshare.7914365.v2. URL: https://figshare.com/articles/10_years_average_run_W_O-/7914365/2.

Dussin, R., Curchitser, E., Stock, C.A., Van Oostende, N., 2019h. 10 years average run w+o-n+. https://doi.org/10.6084/m9.figshare.7914395.v2. URL: https://figshare.com/articles/10_years_average_run_W_O-/7914395/2.

Elrod, V.A., Berelson, W.M., Coale, K.H., Johnson, K.S., 2004. The flux of iron from continental shelf sediments: a missing source for global budgets: flux of iron from the continental shelf. Geophys. Res. Lett. 31, L12307. https://doi.org/10.1029/2004GL020216. URL: http://doi.wiley.com/10.1029/2004GL020216.

Fan, S.M., Moxim, W.J., Levy, H., 2006. Aeolian input of bioavailable iron to the ocean. Geophys. Res. Lett. 33, L07602. https://doi.org/10.1029/2005GL024852. URL: http://doi.wiley.com/10.1029/2005GL024852.

Frölicher, T.L., Joos, F., Plattner, G.K., Steinacher, M., Doney, S.C., 2009. Natural variability and anthropogenic trends in oceanic oxygen in a coupled carbon cycle-climate model ensemble: variability and trends in oceanic oxygen. Global Biogeochem. Cycles 23 GB1003. https://doi.org/10.1029/2008GB003316. URL: http://doi.wiley.com/10.1029/2008GB003316.

Frölicher, T.L., Rodgers, K.B., Stock, C.A., Cheung, W.W.L., 2016. Sources of uncertainties in 21st century projections of potential ocean ecosystem stressors: uncertainties in stressor projections. Glob. Biogeochem. Cycles 30, 1224–1243. https://doi.org/10.1002/2015GB005338. URL: http://doi.wiley.com/10.1002/2015GB005338.

Fuhrer, G.J., Tanner, D.Q., Morace, J.L., McKenzie, S.W., Skach, K.A., 1996. Water Quality of the Lower Columbia River Basin; Analysis of Current and Historical Water-Quality Data through 1994. https://doi.org/10.3133/wri954294. Technical Report. URL: https://pubs.er.usgs.gov/publication/wri954294.

Garcia, H.E., Locarnini, R.A., Boyer, T.P., Antonov, J.I., Baranova, O., Zweng, M., Reagan, J., Johnson, D., 2014a. World Ocean Atlas 2013, volume 3: dissolved oxygen, apparent oxygen utilization, and oxygen saturation. Technical Report. URL: https://data.nodc.noaa.gov/woa/WOA13/DOC/woa13_vol3.pdf.

Garcia, H.E., Locarnini, R.A., Boyer, T.P., Antonov, J.I., Baranova, O., Zweng, M., Reagan, J., Johnson, D., 2014b. World Ocean Atlas 2013. Dissolved Inorganic Nutrients (phosphate, nitrate, silicate) Volume 4 Technical Report. URL: https://data.nodc.noaa.gov/woa/WOA13/DOC/woa13_vol4.pdf.

Haidvogel, D., Arango, H., Budgell, W., Cornuelle, B., Curchitser, E., Di Lorenzo, E., Fennel, K., Geyer, W., Hermann, A., Lanerolle, L., Levin, J., McWilliams, J., Miller, A., Moore, A., Powell, T., Shchepetkin, A., Sherwood, C., Signell, R., Warner, J., Wilkin, J., 2008. Ocean forecasting in terrain-following coordinates: formulation and skill assessment of the Regional Ocean modeling system. J. Comput. Phys. 227, 3595–3624. https://doi.org/10.1016/j.jcp.2007.06.016. URL: http://linkinghub.elsevier.com/retrieve/pii/S0021999107002549.

Helm, K.P., Bindoff, N.L., Church, J.A., 2011. Observed decreases in oxygen content of the global ocean: global decreases in ocean oxygen levels. Geophys. Res. Lett. 38, L23602. https://doi.org/10.1029/2011GL049513. URL: http://doi.wiley.com/10.1029/2011GL049513.

Hutchins, D.A., DiTullio, G.R., Zhang, Y., Bruland, K.W., 1998. An iron limitation mosaic in the California upwelling regime. Limnol. Oceanogr. 43, 1037–1054. https://doi.org/10.4319/lo.1998.43.6.1037. URL: http://doi.wiley.com/10.4319/lo.1998.43.6.1037.

Irby, I., 2018. Associated dataset: the competing impacts of climate change and nutrient reductions on dissolved oxygen in Chesapeake Bay. URL: https://publish.wm.edu/data/154/ . type: dataset.

Jacox, M.G., Edwards, C.A., 2011. Effects of stratification and shelf slope on nutrient supply in coastal upwelling regions. J. Geophys. Res. 116, C03019. https://doi.org/10.1029/2010JC006547. URL: http://doi.wiley.com/10.1029/2010JC006547.

Jacox, M.G., Edwards, C.A., 2012. Upwelling source depth in the presence of nearshore wind stress curl: curl-driven upwelling. J. Geophys. Res. Oceans 117, C05008. https://doi.org/10.1029/2011JC007856. URL: http://doi.wiley.com/10.1029/2011JC007856.

Jacox, M.G., Fiechter, J., Moore, A.M., Edwards, C.A., 2015. ENSO and the California Current coastal upwelling response. J. Geophys. Res. Oceans 120, 1691–1702. https://doi.org/10.1002/2014JC010650. URL: http://doi.wiley.com/10.1002/2014JC010650.

John, J.G., Stock, C.A., Dunne, J.P., 2015. A more productive, but different, ocean after mitigation: altered ocean after mitigation. Geophys. Res. Lett. 42, 9836–9845. https://doi.org/10.1002/2015GL066160. URL: http://doi.wiley.com/10.1002/2015GL066160.

Kahru, M., Kudela, R., Manzano-Sarabia, M., Mitchell, B.G., 2009. Trends in primary production in the California Current detected with satellite data. J. Geophys. Res. 114, C02004. https://doi.org/10.1029/2008JC004979. URL: http://doi.wiley.com/10.1029/2008JC004979.

Keeling, R.F., Garcia, H.E., 2002. The change in oceanic O2 inventory associated with recent global warming. Proc. Natl. Acad. Sci. Unit. States Am. 99, 7848–7853. https://doi.org/10.1073/pnas.122154899. URL: http://www.pnas.org/cgi/doi/10.1073/pnas.122154899.

Keeling, R.F., Körtzinger, A., Gruber, N., 2010. Ocean deoxygenation in a warming world. Ann. Rev. Mar. Sci. 2, 199–229. https://doi.org/10.1146/annurev.marine.010908.163855. URL: http://www.annualreviews.org/doi/10.1146/annurev.marine.010908.163855.

Keller, A.A., Ciannelli, L., Wakefield, W.W., Simon, V., Barth, J.A., Pierce, S.D., 2015. Occurrence of demersal fishes in relation to near-bottom oxygen levels within the California Current large marine ecosystem. Fish. Oceanogr. 24, 162–176. https://doi.org/10.1111/fog.12100. URL: http://doi.wiley.com/10.1111/fog.12100.

Key, R.M., Kozyr, A., Sabine, C.L., Lee, K., Wanninkhof, R., Bullister, J.L., Feely, R.A., Millero, F.J., Mordy, C., Peng, T.H., 2004. A global ocean carbon climatology: results from global ocean data analysis project (glodap). Global Biogeochem. Cycles 18 GB4031. https://doi.org/10.1029/2004GB002247. URL: http://doi.wiley.com/10.1029/2004GB002247.

Large, W.G., Yeager, S.G., 2004. Diurnal to decadal global forcing for ocean and sea-ice models: the data sets and flux climatologies. NCAR Technical note. URL: http://opensky.ucar.edu/islandora/object/technotes 434.

Lohan, M.C., Bruland, K.W., 2006. Importance of vertical mixing for additional sources of nitrate and iron to surface waters of the Columbia River plume: implications for biology. Mar. Chem. 98, 260–273. https://doi.org/10.1016/j.marchem.2005.10.003. URL: http://linkinghub.elsevier.com/retrieve/pii/S0304420305001428.

Manizza, M., 2005. Bio-optical feedbacks among phytoplankton, upper ocean physics and sea-ice in a global model. Geophys. Res. Lett. 32, L05603. https://doi.org/10.1029/2004GL020778. URL: http://doi.wiley.com/10.1029/2004GL020778.

Moxim, W.J., Fan, S.M., Levy, H., 2011. The meteorological nature of variable soluble iron transport and deposition within the North Atlantic Ocean basin. J. Geophys. Res. 116, D03203. https://doi.org/10.1029/2010JD014709. URL: http://doi.wiley.com/10.1029/2010JD014709.

NASA Ocean Biology Processing Group, 2015. SeaWiFS Level 3 Binned Chlorophyll Data Version 2014.

Renault, L., Deutsch, C., McWilliams, J.C., Frenzel, H., Liang, J.H., Colas, F., 2016. Partial decoupling of primary productivity from upwelling in the California Current system. Nat. Geosci. 9, 505–508. https://doi.org/10.1038/ngeo2722. URL: http://www.nature.com/doifinder/10.1038/ngeo2722.

Reynolds, R.W., Rayner, N.A., Smith, T.M., Stokes, D.C., Wang, W., 2002. An improved in situ and satellite SST analysis for climate. J. Clim. 15, 1609–1625. https://doi.org/10.1175/1520-0442. URL: http://journals.ametsoc.org/doi/abs/10.1175/1520-0442%282002%29015%3C1609%3AAIISAS%3E2.0.CO%3B2 (2002) 015 < 1609:AIISAS > 2.0.CO;2.

Rienecker, M.M., Suarez, M.J., Gelaro, R., Todling, R., Bacmeister, J., Liu, E., Bosilovich, M.G., Schubert, S.D., Takacs, L., Kim, G.K., Bloom, S., Chen, J., Collins, D., Conaty, A., da Silva, A., Gu, W., Joiner, J., Koster, R.D., Lucchesi, R., Molod, A., Owens, T.,

Pawson, S., Pegion, P., Redder, C.R., Reichle, R., Robertson, F.R., Ruddick, A.G., Sienkiewicz, M., Woollen, J., 2011. MERRA: NASA's modern-era retrospective analysis for research and applications. J. Clim. 24, 3624–3648. https://doi.org/10.1175/JCLI-D-11-00015.1. URL: http://journals.ametsoc.org/doi/abs/10.1175/JCLI-D-11-00015.1.

Rykaczewski, R.R., Dunne, J.P., 2010. Enhanced nutrient supply to the California current ecosystem with global warming and increased stratification in an earth system model: future nutrient supply to the cce. Geophys. Res. Lett. 37, L21606. https://doi.org/10.1029/2010GL045019. URL: http://doi.wiley.com/10.1029/2010GL045019.

Rykaczewski, R.R., Dunne, J.P., Sydeman, W.J., García-Reyes, M., Black, B.A., Bograd, S.J., 2015. Poleward displacement of coastal upwelling-favorable winds in the ocean's eastern boundary currents through the 21st century: upwelling responses to climate change. Geophys. Res. Lett. 42, 6424–6431. https://doi.org/10.1002/2015GL064694. URL: http://doi.wiley.com/10.1002/2015GL064694.

Schmidtko, S., Stramma, L., Visbeck, M., 2017. Decline in global oceanic oxygen content during the past five decades. Nature 542, 335–339. https://doi.org/10.1038/nature21399. URL: http://www.nature.com/doifinder/10.1038/nature21399.

Seitzinger, S.P., Harrison, J.A., Dumont, E., Beusen, A.H.W., Bouwman, A.F., 2005. Sources and delivery of carbon, nitrogen, and phosphorus to the coastal zone: an overview of global nutrient export from watersheds (news) models and their application: global export of C, N, and P to coastal systems. Global Biogeochem. Cycles 19 GB4S01. https://doi.org/10.1029/2005GB002606. URL: http://doi.wiley.com/10.1029/2005GB002606.

Shchepetkin, A.F., McWilliams, J.C., 2005. The regional oceanic modeling system (ROMS): a split-explicit, free-surface, topography-following-coordinate oceanic model. Ocean Model. 9, 347–404. https://doi.org/10.1016/j.ocemod.2004.08.002. URL: http://linkinghub.elsevier.com/retrieve/pii/S1463500304000484.

Snyder, M.A., Sloan, L.C., Diffenbaugh, N.S., Bell, J.L., 2003. Future climate change and upwelling in the California Current. Geophys. Res. Lett. 30, 1823. https://doi.org/10.1029/2003GL017647. URL: http://doi.wiley.com/10.1029/2003GL017647.

Song, H., Miller, A.J., Cornuelle, B.D., Di Lorenzo, E., 2011. Changes in upwelling and its water sources in the California Current System driven by different wind forcing. Dyn. Atmos. Oceans 52, 170–191. https://doi.org/10.1016/j.dynatmoce.2011.03.001. URL: https://linkinghub.elsevier.com/retrieve/pii/S0377026511000091.

Stock, C.A., Alexander, M.A., Bond, N.A., Brander, K.M., Cheung, W.W., Curchitser, E.N., Delworth, T.L., Dunne, J.P., Griffies, S.M., Haltuch, M.A., Hare, J.A., Hollowed, A.B., Lehodey, P., Levin, S.A., Link, J.S., Rose, K.A., Rykaczewski, R.R., Sarmiento, J.L., Stouffer, R.J., Schwing, F.B., Vecchi, G.A., Werner, F.E., 2011. On the use of IPCC-class models to assess the impact of climate on Living Marine Resources. Prog.

Oceanogr. 88, 1–27. https://doi.org/10.1016/j.pocean.2010.09.001. URL: http://linkinghub.elsevier.com/retrieve/pii/S0079661110001096.

Stock, C.A., Dunne, J.P., John, J.G., 2014. Global-scale carbon and energy flows through the marine planktonic food web: an analysis with a coupled physical–biological model. Prog. Oceanogr. 120, 1–28. https://doi.org/10.1016/j.pocean.2013.07.001. URL: http://linkinghub.elsevier.com/retrieve/pii/S0079661113001079.

Sydeman, W.J., Garcia-Reyes, M., Schoeman, D.S., Rykaczewski, R.R., Thompson, S.A., Black, B.A., Bograd, S.J., 2014. Climate change and wind intensification in coastal upwelling ecosystems. Science 345, 77–80. https://doi.org/10.1126/science.1251635. URL: http://www.sciencemag.org/cgi/doi/10.1126/science.1251635.

Tagliabue, A., Aumont, O., DeAth, R., Dunne, J.P., Dutkiewicz, S., Galbraith, E., Misumi, K., Moore, J.K., Ridgwell, A., Sherman, E., Stock, C., Vichi, M., Völker, C., Yool, A., 2016. How well do global ocean biogeochemistry models simulate dissolved iron distributions? Glob. Biogeochem. Cycles 30, 149–174. https://doi.org/10.1002/2015GB005289. URL: http://doi.wiley.com/10.1002/2015GB005289.

Tagliabue, A., Bowie, A.R., Boyd, P.W., Buck, K.N., Johnson, K.S., Saito, M.A., 2017. The integral role of iron in ocean biogeochemistry. Nature 543, 51–59. https://doi.org/10.1038/nature21058. URL: http://www.nature.com/articles/nature21058.

Till, C.P., Solomon, J.R., Cohen, N.R., Lampe, R.H., Marchetti, A., Coale, T.H., Bruland, K.W., 2018. The iron limitation mosaic in the California Current System: factors governing Fe availability in the shelf/near-shelf region: factors governing Fe availability. Limnol. Oceanogr. 109–123 https://doi.org/10.1002/lno.11022. URL. http://doi.wiley.com/10.1002/lno.11022.

Turi, G., Alexander, M., Lovenduski, N.S., Capotondi, A., Scott, J., Stock, C., Dunne, J., John, J., Jacox, M., 2018. Response of O2 and pH to ENSO in the California Current System in a high-resolution global climate model. Ocean Sci. 14, 69–86. https://doi.org/10.5194/os-14-69-2018. URL: https://www.ocean-sci.net/14/69/2018/.

Van Oostende, N., Dussin, R., Stock, C., Barton, A., Curchitser, E., Dunne, J., Ward, B., 2018. Simulating the ocean's chlorophyll dynamic range from coastal upwelling to oligotrophy. Prog. Oceanogr. 168, 232–247. https://doi.org/10.1016/j.pocean.2018.10.009. URL: https://linkinghub.elsevier.com/retrieve/pii/S0079661117302586.

Wanninkhof, R., 1992. Relationship between wind speed and gas exchange. J. Geophys. Res. 97, 7373–7382. https://doi.org/10.1029/92JC00188. URL: https://agupubs.onlinelibrary.wiley.com/doi/abs/10.1029/92JC00188.

Xiu, P., Chai, F., Curchitser, E.N., Castruccio, F.S., 2018. Future changes in coastal upwelling ecosystems with global warming: the case of the California Current System. Sci. Rep. 8 https://doi.org/10.1038/s41598-018-21247-7. URL: http://www.nature.com/articles/s41598-018-21247-7.